



Materials that can replace liquid electrolytes in Li batteries: Superionic conductivities in $\text{Li}_{1.7}\text{Al}_{0.3}\text{Ti}_{1.7}\text{Si}_{0.4}\text{P}_{2.6}\text{O}_{12}$. Processing combustion synthesized nanopowders to free standing thin films

Eongyu Yi^a, Weimin Wang^a, Som Mohanty^b, John Kieffer^a, Ryo Tamaki^b, Richard M. Laine^{a, c, *}

^a Department of Materials Science and Engineering, University of Michigan, Ann Arbor, MI 48109-2136, USA

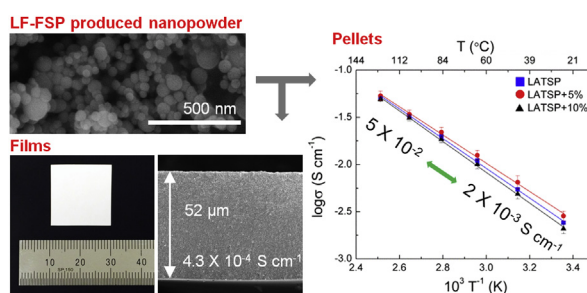
^b Quallion LLC, 12744 San Fernando Road, Sylmar, CA 91342, USA

^c Macromolecular Science and Engineering, University of Michigan, USA

HIGHLIGHTS

- LF-FSP produces non-aggregated nanopowders, excellent feedstock to tape cast.
- $\text{Li}_{1.7}\text{Al}_{0.3}\text{Ti}_{1.7}\text{Si}_{0.4}\text{P}_{2.6}\text{O}_{12}$ pellets with conductivities $>10^{-3} \text{ S cm}^{-1}$ (25 °C).
- Excess Li addition lowers sintering temperatures but has no effect on conductivities.
- Thin films (52 μm) with conductivities of $4.3 \times 10^{-4} \text{ S cm}^{-1}$ (25 °C).

GRAPHICAL ABSTRACT



ARTICLE INFO

Article history:

Received 17 April 2014

Received in revised form

3 July 2014

Accepted 4 July 2014

Available online 12 July 2014

Keywords:

Nanopowder

Superionic

Solid electrolyte

Thin film

Lithium ion battery

ABSTRACT

We demonstrate that liquid-feed flame spray pyrolysis (LF-FSP) processing provides non-aggregated nanopowders that can be used immediately to tape cast, producing thin films ($<100 \mu\text{m}$) of Li^+ ion conducting membranes when sintered. Glass-ceramic or sol–gel processing methods are commonly used for such but require additional high-energy milling and/or calcining to obtain powder feedstock. $\text{Li}_{1+x+y}\text{Al}_x\text{Ti}_{2-x}\text{Si}_y\text{P}_{3-y}\text{O}_{12}$ ($x = 0.1, 0.3/y = 0.2, 0.4$) nanopowders were prepared by LF-FSP with a primary focus on the effects of $\text{Al}_{0.3}/\text{Si}_{0.4}$ doping on conductivities. Furthermore, the effects of excess Li_2O on $\text{Al}_{0.3}/\text{Si}_{0.4}$ doped materials were studied. $\text{Li}_{1.7}\text{Al}_{0.3}\text{Ti}_{1.7}\text{Si}_{0.4}\text{P}_{2.6}\text{O}_{12}$ pellets sintered to 93–94% of theoretical density and samples with varying excess Li_2O contents all show superionic conductivities of $2-3 \times 10^{-3} \text{ S cm}^{-1}$ at room temperature. Li_2O lowers both the crystallization temperatures and temperatures required to sinter. Total conductivities range from 2×10^{-3} to $5 \times 10^{-2} \text{ S cm}^{-1}$ in the temperature span of 25°–125 °C. Small grain sizes of $600 \pm 200 \text{ nm}$ were produced. Initial attempts to make thin films gave films with thicknesses of $52 \pm 1 \mu\text{m}$ on sintering just to 1000 °C. Measured conductivities were $3-5 \times 10^{-4} \text{ S cm}^{-1}$; attributed to final densities of only $\approx 88\%$.

© 2014 Elsevier B.V. All rights reserved.

1. Introduction

Lithium ion batteries are of great interest due to their ability to offer high energy densities and excellent cycle life [1–4]. As such, they are now found extensively in commercial devices ranging

* Corresponding author. Department of Materials Science and Engineering, University of Michigan, Ann Arbor, MI 48109-2136, USA. Tel.: +1 734 764 6203; fax: +1 734 763 4788.

E-mail address: talsdad@umich.edu (R.M. Laine).

from portable electronics to hybrid electric (HEV) and/or electric vehicles (EV) [5–8]. Rapid growth of the lithium battery market is expected to continue given that HEV/EV applications are relatively young, and new potential applications are emerging such as energy storage systems (ESS) for harnessed renewable energies [5,7,8].

Although lithium ion battery technology is now well established and has matured considerably over the past several decades; [2,3,5,7] even with current lithium batteries, safety concerns persist due to potential fire hazards especially those resulting from flammable liquid organic electrolytes used currently, mandating development of more reliable electrolytes [9]. Abuse or manufacturing defects can result in over-charge/discharge or internal shorts, causing electrolyte to decompose or to react exothermically with electrodes [10–12]. If the temperature exceeds the melting point of the separators (130–150 °C) used to prevent contact between the cathode and anode, internal shorts can form with excessive heat output. [13] In some instances, more heat is generated than can be dissipated, resulting in thermal runaway, fires, smoke, and explosions in extreme cases [14,15]. Coincident pressure buildup within the battery pack can cause further mechanical failure within the cell and internal short circuits. [11,12,15] Larger fires or explosions can be envisioned when HEV/EV/ESS lithium batteries fail as the volumes are much greater compared to those of portable electronic devices [7].

Granted, the likelihood of a lithium battery failure is very low due to strengthened safety regulations and improved safety mechanisms over the past decades [12]. However, concerns continue since lithium ion batteries are expected to serve as primary energy storage devices, replacing batteries based on different chemistries [5,7,8]. Thus, all solid state batteries are sought as alternatives. Both polymer [16–18] and ceramic [18,19] replacements for liquid electrolytes are under intense investigation with ceramic electrolytes considered to be the safest as they offer higher thermal stability and Young's moduli. For high performance, solid electrolytes with conductivities comparable to organic electrolytes ($>10^{-3}$ S cm $^{-1}$) are required [20,21].

LiTi $_2$ (PO $_4$) $_3$ (LTP), one of the most widely studied lithium conducting materials, has a NASICON (sodium super ionic conductor) type structure where corner sharing PO $_4$ tetrahedra and TiO $_6$ octahedra networks form the crystal structure framework [22–24]. Two interstitial sites, labeled M1 and M2 are considered for Li $^+$ ion conduction. For pure LTP, only M1 sites are fully occupied by Li $^+$ ions [22,24]. The conduction of Li $^+$ ions is a diffusional process wherein Li $^+$ ions hop from one site to a neighboring site [22].

Pioneering studies by Aono et al. [25] explored doping of LiTi $_2$ (PO $_4$) $_3$ by partially substituting Ti $^{4+}$ or P $^{5+}$ sites with other cations to reach higher total conductivities. Of the materials they studied, Li $_{1+x}$ M $_x$ Ti $_{2-x}$ (PO $_4$) $_3$ (M $^{3+}$ = Al $^{3+}$, Sc $^{3+}$) had the highest conductivity, 7×10^{-4} S cm $^{-1}$ at 25 °C. The dramatic increases observed from 2×10^{-6} S cm $^{-1}$ for undoped to 7×10^{-4} S cm $^{-1}$ in doped material were ascribed primarily to improved densification of the doped materials. Their work prompted many further studies on Al $^{3+}$ doping of LiTi $_2$ (PO $_4$) $_3$ [26–32]. Other doping studies targeting higher conductivities include substitution of Ge $^{4+}$ on Ti $^{4+}$ sites, and V $^{5+}$ or Nb $^{5+}$ on P $^{5+}$ sites [29,33,34]. The overall conclusion is that the final densities of sintered pellets, [25,29,31] the activation energies of Li $^+$ conduction, [28,33] the presence of secondary phases, [29,33] and the average grain sizes [31,32,35] influence Li $^+$ conductivities.

Superionic conductivities ($>10^{-3}$ S cm $^{-1}$) are typical for Li $_{1.3}$ Al $_{0.3}$ Ti $_{1.7}$ (PO $_4$) $_3$ or Li $_{1.5}$ Al $_{0.5}$ Ge $_{1.5}$ (PO $_4$) $_3$ materials made by glass-ceramic processing [28,36,37]. However, the thicknesses of sheets made this way (1–2 mm) limit gravimetric/volumetric energy densities and are not applicable to actual devices. In order to process thin films (<100 μ m), glass sheets are crushed and ball milled

to produce powders with properties acceptable for tape casting, and thereafter sintered [36,38,39].

The motivation for the current work was to synthesize lithium conducting nanopowders in a single step using liquid-feed flame spray pyrolysis (LF–FSP) thereby eliminating the glass forming, crushing, and ball milling steps. Furthermore, nanopowders offer potential access to finer final grain sizes potentially crucial to obtaining higher conductivities [31,32,35].

We have investigated co-doping of Al $^{3+}$ and Si $^{4+}$ in LiTi $_2$ (PO $_4$) $_3$ since examples of such materials are rare [40,41] despite Fu's [40] report showing superionic conductivities of 1.5×10^{-3} S cm $^{-1}$. Most of the work reported here focuses on Li $_{1.7}$ Al $_{0.3}$ Ti $_{1.7}$ Si $_{0.4}$ P $_{2.6}$ O $_{12}$, which showed the highest conductivities among compositions surveyed. Li $_2$ O is introduced to Li $_{1.7}$ Al $_{0.3}$ Ti $_{1.7}$ Si $_{0.4}$ P $_{2.6}$ O $_{12}$ as a sintering aid, which may cause liquid phase sintering [42–44]. In addition, based on our findings, initial studies were undertaken to process thin films (50–70 μ m) from these powders given that such thicknesses would be ideal for lithium batteries of all types.

2. Experimental

2.1. Materials

Lithium hydroxide monohydrate [LiOH·H $_2$ O], tetraethoxysilane [Si(OC $_2$ H $_5$) $_4$], triethyl phosphate [(C $_2$ H $_5$ O) $_3$ PO], triethanolamine [N(CH $_2$ CH $_2$ OH) $_3$], propionic acid [CH $_3$ CH $_2$ COOH], polyethylene glycol [H(OCH $_2$ CH $_2$) $_n$ OH, M $_n$ = 3400], polyacrylic acid [(C $_3$ H $_4$ O $_2$) $_n$, M $_n$ = 2000], methyl ethyl ketone [C $_2$ H $_5$ COCH $_3$] and benzyl butyl phthalate {2-[CH $_3$ (CH $_2$) $_3$ O $_2$ C]C $_6$ H $_4$ CO $_2$ CH $_2$ C $_6$ H $_5$, 98%} were purchased from Sigma–Aldrich (Milwaukee, WI). Polyvinyl butyral [(C $_8$ H $_{14}$ O $_2$) $_n$, B-98, M $_n$ = 40,000–70,000] was purchased from Butvar (Avon, OH). Titanium isopropoxide [Ti(OiPr) $_4$] was purchased from Fischer Scientific (Pittsburgh, PA), aluminum tri-sec-butoxide [Al{OCH(CH $_3$)CH $_2$ CH $_3$ } $_3$] was purchased from Chattem Chemicals (Chattanooga, TN), and absolute ethanol from Decon Labs (King of Prussia, PA).

2.2. Precursor synthesis

2.2.1. Lithium propionate [LiO $_2$ CCH $_2$ CH $_3$]

[LiOH·H $_2$ O, 113 g, 2.7 mole] was reacted with excess [CH $_3$ CH $_2$ COOH, 500 ml, 6.8 mole] in a 1 L flask equipped with a still head. The solution was heated at 130 °C for 2 h with magnetic stirring until transparent liquid was obtained. On cooling to room temperature, [LiO $_2$ CCH $_2$ CH $_3$] crystallized and was filtered out. The ceramic yield of the resulting precursor was 42 wt %, lower than its theoretical value 44 wt %, as determined by TGA. The discrepancy arises from residual propionic acid. No further purification was done to remove this excess.

2.2.2. Alumatrane [Al{OCH $_2$ CH $_2$ } $_3$ N]

[{Al{OCH(CH $_3$)CH $_2$ CH $_3$ } $_3$ }, 1700 ml, 6.7 mole] was reacted with [N(CH $_2$ CH $_2$ OH) $_3$, 885 ml, 6.7 mole] at a molar ratio of 1 to 1, in a 4 L vessel under N $_2$ flow. [N(CH $_2$ CH $_2$ OH) $_3$] was added slowly via addition funnel while the mixture was stirred constantly over a 4 h period. The resulting alumatrane, dissolved in byproduct butanol, had a TGA determined ceramic yield of 12 wt %.

2.2.3. Titanatrane glycolate {Ti{OCH $_2$ CH $_2$ } $_3$ N

[OCH $_2$ CH $_2$ N(CH $_2$ CH $_2$ OH) $_2$]

[Ti(OiPr) $_4$, 1150 ml, 3.80 mole] was reacted with [N(CH $_2$ CH $_2$ OH) $_3$, 1010 ml, 7.60 mole] at a molar ratio of 1–2, in an identical method to that described above. The resulting titanatrane glycolate, dissolved in byproduct isopropanol, had a TGA determined ceramic yield of 13 wt %.

2.3. Liquid-feed flame spray pyrolysis (LF-FSP)

In this study, lithium propionate, alumatrane, titanatrane glycolate, tetraethoxysilane, and triethyl phosphate were dissolved in ethanol at selected molar ratios to give a 3 wt % ceramic yield solution. The resulting solution was subsequently aerosolized with oxygen into a quartz chamber where it was ignited with methane/oxygen pilot torches. Produced powders were collected downstream in rod-in-tube electrostatic precipitators (ESP) operated at 10 kV. Details of the LF-FSP process including particle formation mechanism and metalloorganic precursor studies can be found elsewhere [45–49].

Unfortunately, initial attempts resulted in powders with significant amounts of TiP_2O_7 when crystallized, which we ascribed to Li shortages arising from the volatility of Li_2O from flame temperatures $>1000^\circ\text{C}$. Several runs were conducted to establish Li loss factors targeting the production of pure $\text{LiTi}_2(\text{PO}_4)_3$ leading to a value of 1.3. Thus, pure $\text{LiTi}_2(\text{PO}_4)_3$ forms when the lithium propionate content is 130% of that needed based simply on precursor stoichiometries. This factor was used in all subsequent studies discussed below.

$\text{Li}_{1+x+y}\text{Al}_x\text{Ti}_{2-x}\text{Si}_y\text{P}_{3-y}\text{O}_{12}$ ($x = 0.1, 0.3/y = 0.2, 0.4$) were synthesized to determine which composition showed the highest potential to reach superionic conductivity. Once $\text{Li}_{1.7}\text{Al}_{0.3}\text{Ti}_{1.7}\text{Si}_{0.4}\text{P}_{2.6}\text{O}_{12}$ was shown to have the highest conductivity, another powder with 10 wt% excess lithium, with respect to the stoichiometric amount of lithium, was produced by dissolving excess lithium propionate in precursor solution to investigate the effect of lithium content, hereafter referred to as LATSP and LATSP+10% respectively.

Table 1 lists the amounts of precursors dissolved in 2760 g (3500 ml) of ethanol for each composition.

2.4. Powder treatment and pellet compaction

The as-produced $\text{Li}_{1+x+y}\text{Al}_x\text{Ti}_{2-x}\text{Si}_y\text{P}_{3-y}\text{O}_{12}$ ($x = 0.1, 0.3/y = 0.2, 0.4$) powders which were used for preliminary experiments were pressed in a dual action 14.2 mm WC die. No further treatment of the powder or pressing was done to improve green densities.

Additional steps were adopted to enhance the LATSP and LATSP+10% green densities to optimize final, sintered densities and ionic conductivities. Selected amount of as-produced powders (18 g) were dispersed in ethanol (300 ml) with an ultrasonic horn (Vibra cell VC-505, Sonics and Materials, Inc., Newton, CT) at 100 W for 15 min and left for 24 h to allow larger particles to settle. The suspension was decanted, dried, re-dispersed (100 W, 15 min) in ethanol (300 ml) with addition of 4 wt %, with respect to powder mass, of poly ethylene glycol, and dried again. The resulting powders were ground in an alumina mortar and pestle, and subsequently sieved through 80 μm nylon mesh. The granulated powders (350 mg) were pressed in a dual action 14.2 mm WC die, followed by cold isostatic pressing (Autoclave engineers, Erie, PA) at 200 MPa for 30 min.

$\text{Li}_{1.7}\text{Al}_{0.3}\text{Ti}_{1.7}\text{Si}_{0.4}\text{P}_{2.6}\text{O}_{12}$ with 5% excess lithium (LATSP+5%) was formulated by mixing LATSP and LATSP+10% in a 1:1 wt. ratio by

Table 2

Starting materials and composition for film casting.

	Role	Mass (g)	wt. %	vol. %
LATSP+5%	Powder	1.00	30	12
Benzyl butyl phthalate	Plasticizer	0.14	4	4
Polyvinyl butyral	Binder	0.14	4	4
Polyacrylic acid	Dispersant	0.03	1	1
Ethanol	Solvent	0.4	12	16
Methyl ethyl ketone	Solvent	1.6	49	64

ultrasonication (100 W, 15 min). Identical procedures as above were done for pellet compaction.

2.5. Thin film preparation

Table 2 lists the components used to cast films. Powder, dispersant, and solvent were ball-milled with spherical 99% alumina beads with 3.0 mm diameter for 6 h in a 20 ml vial to break up agglomerates and disperse powder. Subsequently, binder and plasticizer were introduced and the new mixture was ball-milled for an additional 24 h to homogenize the suspension. A ball tumbler (Rotary Tumbler Model B, Tru-Square Metal Products, Auburn, WA) was used for milling. One fifth of the container was filled with the milling media.

Suspensions were cast using a wire wound rod coater (Automatic Film Applicator-1137, Sheen Instrument, Ltd, UK). Spacers were placed between the rod and the substrate to maintain a gap of 400 μm . After solvent evaporation, the resulting green films had thicknesses of $\sim 75 \mu\text{m}$. Dried green films were manually peeled off the Mylar substrate, and cut to $2.5 \times 2.5 \text{ cm}$.

2.6. Crystallization and sintering

Heat treatments were conducted in a Lindberg/Blue M single zone tube furnace (Watertown, WI). For quick tests of $\text{Li}_{1+x+y}\text{Al}_x\text{Ti}_{2-x}\text{Si}_y\text{P}_{3-y}\text{O}_{12}$ ($x = 0.1, 0.3/y = 0.2, 0.4$) samples, pellets were heated to 900° , 1000° , 1100° , and 1200°C at a ramp rate of 5°C min^{-1} and held for 1 h. For LATSP with varying lithium content studies, green pellets were heated to 690° , 680° , and 660°C at a ramp rate of 5°C min^{-1} for LATSP, LATSP+5%, and LATSP+10% respectively. The temperature was held for 1 h at constant air flow of 60 ml min^{-1} . Crystallized pellets of LATSP, LATSP+5% and LATSP+10% were sintered at 1200° , 1180° , and 1140°C respectively for 1 h under 60 ml min^{-1} air flow. The ramp rate was 5°C min^{-1} to 700°C and 1°C min^{-1} to the target temperature. For film studies, green films were placed in between alumina plates and debinded/crystallized at 665°C for 2 h at a ramp rate of 5°C min^{-1} followed by sintering at 1000°C for 1 h at a ramp rate of 1°C min^{-1} . Alumina plates were used to prevent warping. Sintering temperatures were limited to 1000°C as LATSP films sintered onto alumina plates at higher temperatures.

2.7. Polishing and thermal etching of sintered pellets

For SEM imaging, sintered pellets were ground and polished using a Leco Spectrum System 1000 Grinder/Polisher (St. Joseph,

Table 1

Amount of precursors dissolved in ethanol for each composition. (Unit: g).

	Lithium propionate	Alumatrane	Titanatrane glycolate	Tetraethoxysilane	Triethyl phosphate
$\text{Li}_{1.3}\text{Al}_{0.1}\text{Ti}_{1.9}\text{Si}_{0.2}\text{P}_{2.8}\text{O}_{12}$	12.9	9.1	251.4	8.9	109.8
$\text{Li}_{1.5}\text{Al}_{0.1}\text{Ti}_{1.9}\text{Si}_{0.4}\text{P}_{2.6}\text{O}_{12}$	14.9	9.1	250.9	17.9	101.8
$\text{Li}_{1.5}\text{Al}_{0.3}\text{Ti}_{1.7}\text{Si}_{0.2}\text{P}_{2.8}\text{O}_{12}$	15.0	27.6	226.6	9.0	110.6
$\text{Li}_{1.7}\text{Al}_{0.3}\text{Ti}_{1.7}\text{Si}_{0.4}\text{P}_{2.6}\text{O}_{12}$	17.0	27.6	226.1	18.0	102.5
$\text{Li}_{1.7}\text{Al}_{0.3}\text{Ti}_{1.7}\text{Si}_{0.4}\text{P}_{2.6}\text{O}_{12}$ (10 wt% excess Li)	18.7	27.6	226.1	18.0	102.5

MI). The pellets were initially ground with 1200 grit SiC paper (LECO, St. Joseph, MI), and polished with 9, 3, and 1 μm diamond suspensions (Dexter, MI) subsequently. Polished samples were subject to thermal etching at 900 °C for 3 h.

2.8. Characterization

2.8.1. Density measurements

Green pellet densities were calculated by geometrical methods. Diameter, thickness, and mass were measured. Densities of sintered pellets and films were determined using an Archimedes density determination kit (OHAUS Corp., Parsippany, NJ). Suspended and wet masses were measured with pellets and films boiled in ethanol for 1 h. Dry masses were measured after heating the samples at 90 °C for 3 h.

2.8.2. X-ray diffraction

X-Ray powder diffraction (XRD) analyses were run using a Rigaku Rotating Anode Goniometer (Rigaku Denki., Ltd., Tokyo, Japan). XRD scans were made from 10° to 70° 2 θ , using a scan rate of 2° min⁻¹ in 0.01° increments and Cu K α radiation (1.541 Å) operating at 40 kV and 100 mA. As-produced powders, sintered pellets, and sintered films were characterized by XRD. The sintered pellets and films were pulverized with an agate mortar and pestle. Silicon powder was mixed with ground pellet powder in the same fashion and used as an internal standard for lattice parameter calculations. The Jade program 2010 (Version 1.1.5 from Materials Data, Inc., Livermore CA) was used to refine lattice constants, and to determine the presence of crystallographic phases and their wt. fraction compositions.

2.8.3. N₂ adsorption

Specific surface areas (SSA) were obtained using a Micromeritics ASAP 2020 sorption analyzer. Samples (400 mg) were degassed at 400 °C/5 h. Each analysis was run at -196 °C (77 K) with N₂. The SSAs were determined by the BET multipoint method using ten data points at relative pressures of 0.05–0.30.

2.8.4. Scanning electron microscopy

Micrographs were taken using a FEI NOVA Nanolab system (FEI company, Hillsboro, OR). Powder samples were used as is, sintered pellets were polished/etched, and thin films were fractured for imaging. All samples were sputter coated with gold/palladium using a Technics Hummer IV DC sputtering system (Anatech, Ltd., Alexandria, VA).

2.8.5. Thermogravimetric analyses (TGA)/differential scanning calorimetry (DSC)

Crystallization points of as-produced, amorphous powders were confirmed using a Q600 simultaneous TGA/DSC (TA Instruments, Inc., New Castle, DE). Samples (15–25 mg) were loaded in alumina pans and ramped to 700 °C at a heating rate of 10 °C min⁻¹ to 600 °C and 1 °C min⁻¹ to 700 °C, under constant air flow at 60 ml min⁻¹. The solids loadings of the green films were determined by the same method.

2.8.6. Ionic conductivity measurements

AC impedance data were collected with broadband spectrometer (Novocontrol technologies, Hundsangen, Germany) in a frequency range of 10 MHz to 1 Hz at 25° to 125 °C in increments of 20 °C. All measurements were done at a root mean square voltage of 10 mV. Pellet and film surfaces were gently smoothed with 1200 grit SiC paper (LECO, St. Joseph, MI). Gold electrodes, 1 mm in diameter, were deposited using an SPI sputter coater (SPI Supplies, Inc., West Chester, PA) on one side of the surface whereas the other side was coated in full. Obtained Nyquist plots were fit using EIS spectrum analyzer software [50] to estimate total resistance of samples. Conductivities were calculated using the following equation. Here, d , A_e , and R denote pellet thickness, electrode area, and resistance, respectively.

$$\sigma = d/A_e R \quad (1)$$

Activation energies were calculated from Arrhenius plots using the equations below. Here, A , E_a , R_g , and T corresponds to pre-exponential factor, activation energy, gas constant, and absolute temperature, respectively.

$$\sigma = A \exp(-E_a/R_g T) \quad (2)$$

$$\log \sigma = \log A - (E_a/2.3R_g T) \quad (3)$$

3. Results and discussion

The objectives of the work reported here were to identify nanopowder compositions in the $\text{Li}_{1+x+y}\text{Al}_x\text{Ti}_{2-x}\text{Si}_y\text{P}_{3-y}\text{O}_{12}$ system made by LF-FSP that offer Li superionic conductivities in sintered bodies, and that permit processing thin films for membrane applications.

This section is separated into three parts. The first concerns the brief evaluation of $\text{Li}_{1+x+y}\text{Al}_x\text{Ti}_{2-x}\text{Si}_y\text{P}_{3-y}\text{O}_{12}$ ($x = 0.1, 0.3/y = 0.2, 0.4$) samples to determine which sintered pellet compositions show the highest conductivities. Li^+ ionic conductivities and XRD studies of sintered pellets are discussed.

The second part pertains to composition optimization for conductivity. The effects of sintering temperatures and added excess Li_2O are also explored. Discussions on phase compositions, microstructures, and impedance measurements of sintered pellets are presented.

The third pertains to initial efforts to process thin films. Green and sintered films were characterized by TGA, SEM and XRD. The Li^+ ionic conductivities studies of sintered films follow.

Fig. 1 is a schematic experimental flow chart, divided in three parts as aforementioned.

3.1. $\text{Li}_{1+x+y}\text{Al}_x\text{Ti}_{2-x}\text{Si}_y\text{P}_{3-y}\text{O}_{12}$ ($x = 0.1, 0.3/y = 0.2, 0.4$) compositions

We begin with a global characterization of the as-produced powders including XRD, BET and SEM.

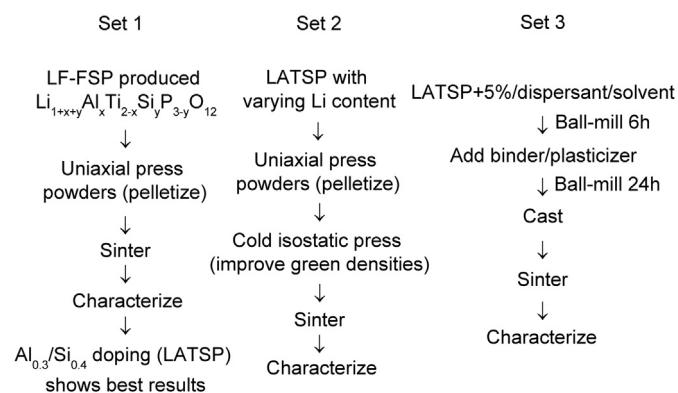


Fig. 1. Schematic experimental flow chart.

3.1.1. As-produced powders

Fig. 2 shows SEM micrographs of as-produced powders of all compositions. For all, spherical particles with APSs <100 nm are observed.

Table 3 lists specific surface areas (SSAs) and average particle sizes (APSs) for as-produced $\text{Li}_{1+x+y}\text{Al}_x\text{Ti}_{2-x}\text{Si}_y\text{P}_{3-y}\text{O}_{12}$ ($x = 0.1, 0.3/y = 0.2, 0.4$) nanopowders. The density of $\text{Li}_2\text{O}-\text{Al}_2\text{O}_3-\text{TiO}_2-\text{P}_2\text{O}_5$ glass, 2.69 g cm^{-3} , was used as an approximation to convert SSAs to APSs. [51] APSs of all powders are <100 nm, consistent with Fig. 2 SEMs.

Fig. 3 provides XRD patterns of as-produced $\text{Li}_{1+x+y}\text{Al}_x\text{Ti}_{2-x}\text{Si}_y\text{P}_{3-y}\text{O}_{12}$ ($x = 0.1, 0.3/y = 0.2, 0.4$) nanopowders. All are amorphous as evidenced by broad humps centered at $\sim 24^\circ 2\theta$.

3.1.2. Sintering and ionic conductivities

Pellets of $\text{Li}_{1+x+y}\text{Al}_x\text{Ti}_{2-x}\text{Si}_y\text{P}_{3-y}\text{O}_{12}$ ($x = 0.1, 0.3/y = 0.2, 0.4$) were heated at $5^\circ \text{C min}^{-1}$ /air and sintered at $900^\circ, 1000^\circ, 1100^\circ$, and 1200°C for 1 h. Fig. 4 shows the XRD patterns of pellets sintered to 1100°C for 1 h. All peaks correspond to those of $\text{LiTi}_2(\text{PO}_4)_3$ for the $\text{Li}_{1.3}\text{Al}_{0.1}\text{Ti}_{1.9}\text{Si}_{0.2}\text{P}_{2.8}\text{O}_{12}$ sample. Small quantities of AlPO_4 and TiO_2 are detected for samples with higher doping concentrations of either Al^{3+} or Si^{4+} . Phase separation/formation of AlPO_4 or TiO_2 is common for these types of material on sintering at $>900^\circ \text{C}$ [40,41,52,53]. No secondary phases related to Si^{4+} are observed.

Fig. 5 presents XRD patterns for $\text{Li}_{1.7}\text{Al}_{0.3}\text{Ti}_{1.7}\text{Si}_{0.4}\text{P}_{2.6}\text{O}_{12}$ pellets sintered to selected temperatures. Pellets sintered at 900°C are mostly phase pure $\text{LiTi}_2(\text{PO}_4)_3$ with small amounts of residual amorphous phase, as evidenced by a small, broad hump at $\sim 24^\circ 2\theta$. Pellets sintered at 1000°C and above are highly crystalline, and AlPO_4 and TiO_2 secondary phases are present. For all $\text{Li}_{1+x+y}\text{Al}_x\text{Ti}_{2-x}\text{Si}_y\text{P}_{3-y}\text{O}_{12}$ ($x = 0.1, 0.3/y = 0.2, 0.4$) samples, higher sintering temperatures resulted in gradual increases in secondary phase peak intensities indicating loss of Li_2O .

Table 3

SSAs and APSs of as-produced $\text{Li}_{1+x+y}\text{Al}_x\text{Ti}_{2-x}\text{Si}_y\text{P}_{3-y}\text{O}_{12}$ ($x = 0.1, 0.3/y = 0.2, 0.4$).

	SSAs ($\text{m}^2 \text{ g}^{-1}$)	APSs (nm)
$\text{Li}_{1.3}\text{Al}_{0.1}\text{Ti}_{1.9}\text{Si}_{0.2}\text{P}_{2.8}\text{O}_{12}$	30	74
$\text{Li}_{1.5}\text{Al}_{0.1}\text{Ti}_{1.9}\text{Si}_{0.4}\text{P}_{2.6}\text{O}_{12}$	35	64
$\text{Li}_{1.5}\text{Al}_{0.3}\text{Ti}_{1.7}\text{Si}_{0.2}\text{P}_{2.8}\text{O}_{12}$	32	70
$\text{Li}_{1.7}\text{Al}_{0.3}\text{Ti}_{1.7}\text{Si}_{0.4}\text{P}_{2.6}\text{O}_{12}$	40	56

Fig. 6 summarizes the room temperature conductivities for $\text{Li}_{1+x+y}\text{Al}_x\text{Ti}_{2-x}\text{Si}_y\text{P}_{3-y}\text{O}_{12}$ ($x = 0.1, 0.3/y = 0.2, 0.4$) pellet samples. These initial samples provided a quick estimate of compositions that show the best potential to reach superionic conductivities. No efforts were made to optimize each composition in terms of densities and conductivities. Rather, all samples were simply pelletized by uni-axial pressing and sintered at selected temperatures and dwell times.

Fig. 6 shows a general trend wherein room temperature conductivities increase with sintering temperature as pellets densify [25]. $\text{Si}_{0.4}$ doped samples offer higher conductivities compared to $\text{Si}_{0.2}$ doped samples. Also, higher doping concentrations result in higher conductivities. Thus $\text{Li}_{1.7}\text{Al}_{0.3}\text{Ti}_{1.7}\text{Si}_{0.4}\text{P}_{2.6}\text{O}_{12}$ shows the highest conductivity at all sintering temperatures. The highest value of $7.7 \times 10^{-4} (\pm 1.5 \times 10^{-4}) \text{ S cm}^{-1}$ is observed for pellets sintered at 1100°C for 1 h.

The next step was to further optimize $\text{Li}_{1.7}\text{Al}_{0.3}\text{Ti}_{1.7}\text{Si}_{0.4}\text{P}_{2.6}\text{O}_{12}$ (LATSP). Thus, pelletized samples were cold isostatically pressed (CIPped) to improve green densities. CIPped pellets had 56% theoretical densities (TD), 10% higher than isostatically pressed pellets. Furthermore, the effects of excess lithium content on overall sintering behavior and conductivity were investigated.

The following section pertains to LATSP synthesized with excess lithium as Li_2O . LATSP+5% and LATSP+10% each denote 5 and 10 wt % excess lithium, respectively. LATSP+10% was synthesized by using

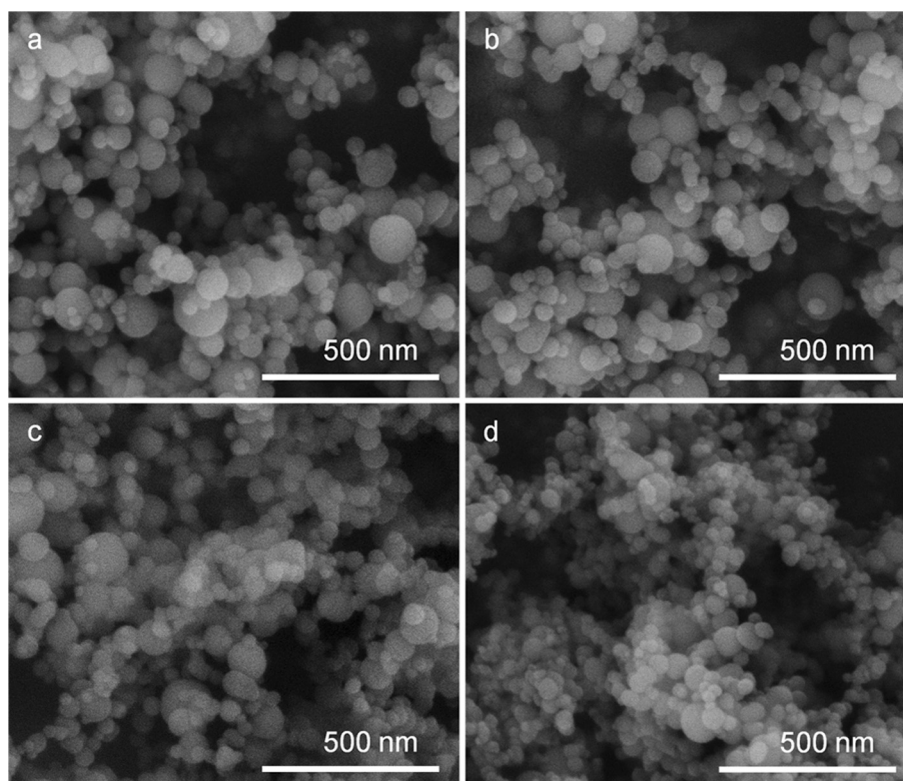


Fig. 2. SEM micrographs of as-produced a. $\text{Al}_{0.1}/\text{Si}_{0.2}$, b. $\text{Al}_{0.1}/\text{Si}_{0.4}$, c. $\text{Al}_{0.3}/\text{Si}_{0.2}$, and d. $\text{Al}_{0.3}/\text{Si}_{0.4}$ nanopowders.

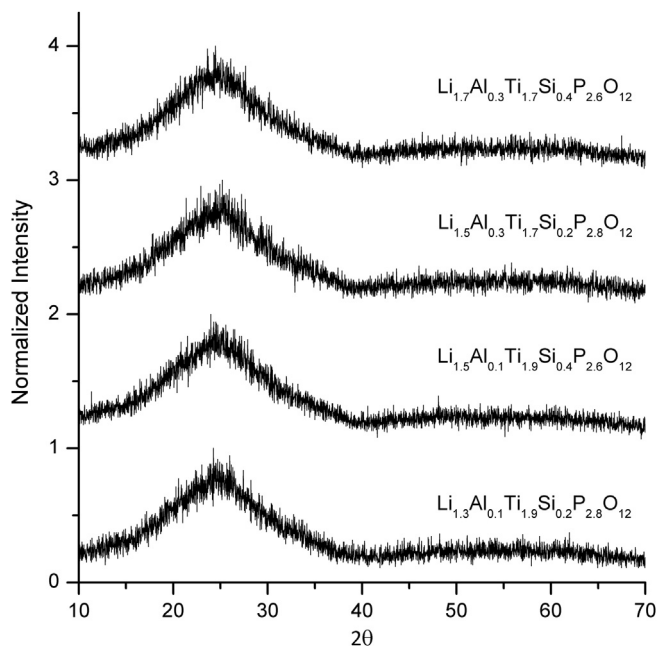


Fig. 3. XRD patterns of as-produced $\text{Li}_{1+x+y}\text{Al}_x\text{Ti}_{2-x}\text{Si}_y\text{P}_{3-y}\text{O}_{12}$ ($x = 0.1, 0.3/y = 0.2, 0.4$).

10 wt% extra lithium propionate compared to the stoichiometric amount, whereas LATSP+5% was made by mixing LATSP and LATSP+10% by ultrasonication. The excess lithium precursor is expected to form Li_2O on heating.

3.2. LATSP/LATSP+5%/LATSP+10%

3.2.1. As-produced powders

Fig. 7 provides XRD patterns of as-produced powders. The broad humps centered at $\sim 24^\circ$ 2θ , observed for both LATSP and LATSP+10% are typical of amorphous samples. Table 4 lists SSAs with APSs determined by N_2 adsorption. Fig. 8 SEMs of as-produced powders show spherical particles with APSs < 100 nm.

The Fig. 9 DSC scans show the crystallization exotherms for LATSP, LATSP+5%, and LATSP+10%. In each sample, only one exotherm is observed for the $\text{LiTi}_2(\text{PO}_4)_3$ phase. The crystallization peak maxima shift from $667 \pm 1^\circ$ to $662 \pm 1^\circ$ and to $656 \pm 1^\circ$ $^\circ\text{C}$ with increasing Li_2O content.

3.2.2. Crystallization and sintering

Thereafter, green pellets were first crystallized at selected temperatures to avoid cracking during crystallization. They were subsequently sintered at higher temperatures for densification. Fig. 10 shows XRD patterns of samples sintered to the highest densities. All peaks correspond to those of $\text{LiTi}_2(\text{PO}_4)_3$ except two assigned to AlPO_4 and TiO_2 .

Table 5 summarizes heating conditions, final densities, and phase compositions of the sintered pellets. Phase compositions were determined by Rietveld refinement using reference files listed in Fig. 10.

Sintering temperatures were reduced by 20° and 60° $^\circ\text{C}$ for LATSP+5% and LATSP+10% pellets respectively, compared to LATSP. The final pellet densities were all ~ 94 %TD, as measured by the Archimedes method. The presence of secondary phases was ignored in these calculations. Longer dwell times or higher

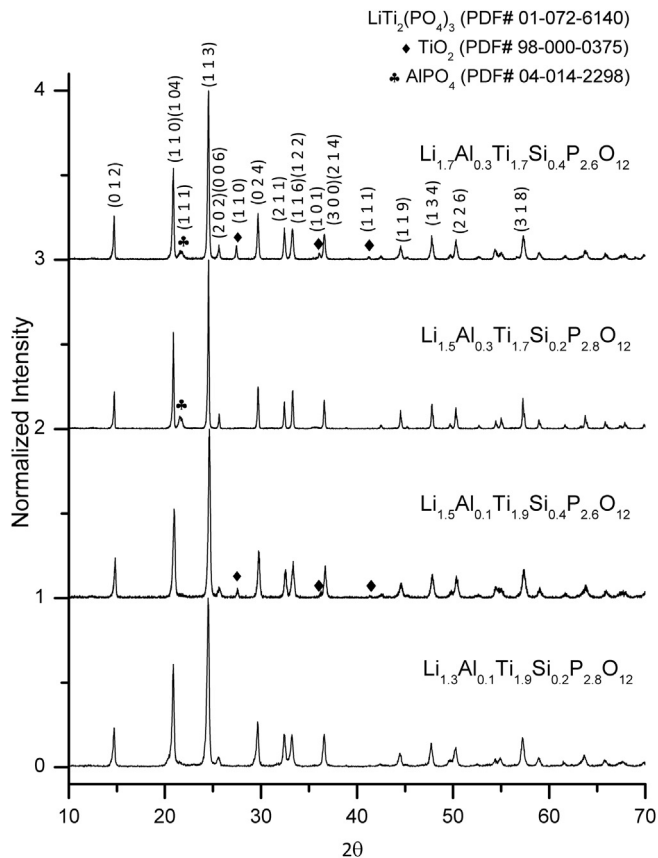


Fig. 4. XRD patterns of $\text{Li}_{1+x+y}\text{Al}_x\text{Ti}_{2-x}\text{Si}_y\text{P}_{3-y}\text{O}_{12}$ ($x = 0.1, 0.3/y = 0.2, 0.4$) pellets sintered at $1100^\circ\text{C}/1$ h. Peaks with no label correspond to $\text{LiTi}_2(\text{PO}_4)_3$.

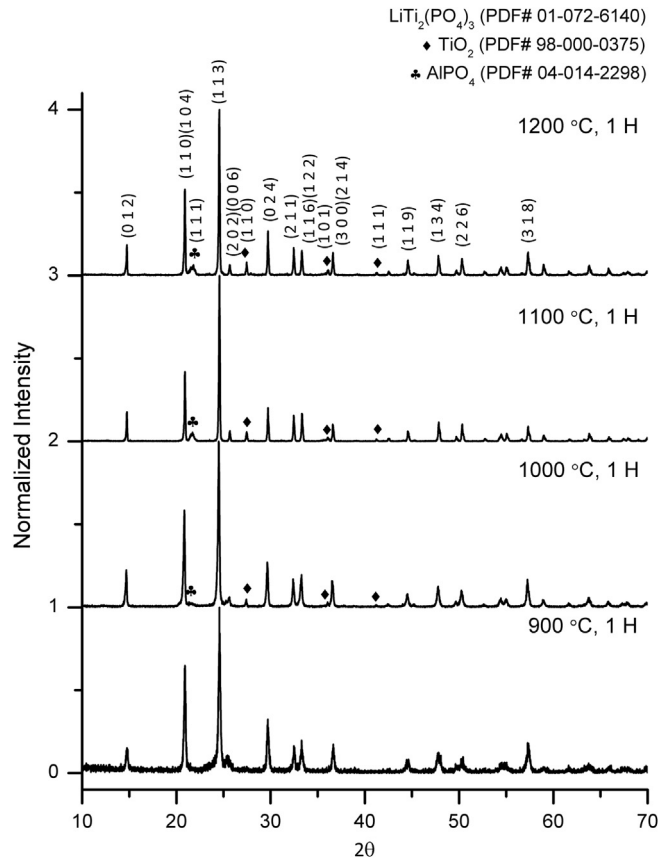


Fig. 5. XRD patterns of $\text{Li}_{1.7}\text{Al}_{0.3}\text{Ti}_{1.7}\text{Si}_{0.4}\text{P}_{2.6}\text{O}_{12}$ pellets sintered at selected temperatures. Peaks with no label correspond to $\text{LiTi}_2(\text{PO}_4)_3$.

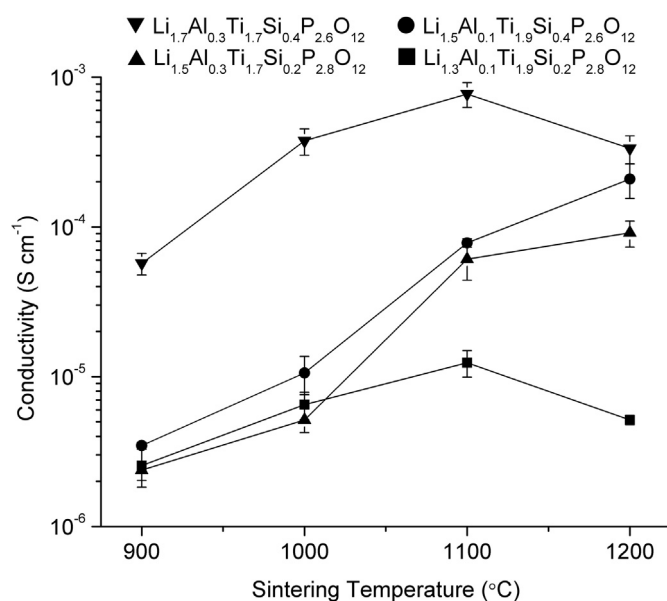


Fig. 6. Room temperature conductivities of samples sintered at selected temperature for 1 h.

temperatures than listed in Table 5 reduced observed densities by 1–3%. These density decreases may be ascribed to the volatility of Li_2O at higher temperatures which promotes formation of secondary phases such as AlPO_4 and TiO_2 [54].

It is rather strange to see similar amounts of AlPO_4 and TiO_2 even when excess lithium is introduced since one would expect it to form $\text{LiTi}_2(\text{PO}_4)_3$ by reacting with AlPO_4 and TiO_2 , hence reducing secondary phase contents. One possible explanation is that the excess Li_2O resides in grain boundaries such that there is a diffusive path, and more of it is lost at lower temperatures compared to stoichiometric samples. The phase compositions of all samples are quite the same, indicating that most of the excess lithium evaporates during sintering.

The LATSP theoretical density is 2.93 g cm^{-3} , as calculated using Table 6 refined lattice parameters. Refinement was done by whole pattern fitting and Rietveld refinement with Jade software using Si (PDF# 98-000-0396) as an internal standard. Table 6 compares the

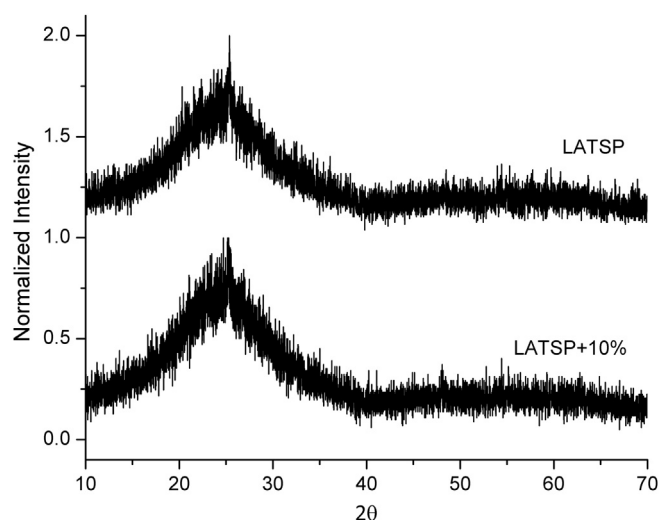


Fig. 7. XRD patterns of as-produced LATSP and LATSP+10% nanopowders.

lattice parameters of LATSP with those of $\text{LiTi}_2(\text{PO}_4)_3$ and $\text{Li}_{1.3}\text{Al}_{0.3}\text{Ti}_{1.7}(\text{PO}_4)_3$. The differences in ionic radii of Al^{3+} (0.535 Å), Ti^{4+} (0.605 Å), Si^{4+} (0.26 Å), and P^{5+} (0.17 Å) explain the changes in lattice parameters [55]. The lattice constants for $\text{Li}_{1.3}\text{Al}_{0.3}\text{Ti}_{1.7}(\text{PO}_4)_3$ are smaller than for $\text{LiTi}_2(\text{PO}_4)_3$ since smaller ionic radius Al^{3+} substitutes for Ti^{4+} , and LATSP has larger lattice parameters compared to $\text{Li}_{1.3}\text{Al}_{0.3}\text{Ti}_{1.7}(\text{PO}_4)_3$ due to substitution of P^{5+} by larger ionic radius Si^{4+} .

3.2.3. Microstructures

Fig. 11 provides the microstructures for samples sintered to the highest densities per Table 5. Average grain sizes (AGSs) determined by the linear intercept method are 625 ± 230 , 590 ± 180 , and $610 \pm 210 \text{ nm}$ for LATSP, LATSP+5% and LATSP+10%, respectively. All samples have very similar AGSs despite being sintered at different temperatures. This suggests that densification and grain growth are triggered at lower temperatures with the addition of excess Li_2O . Li_2O thus must act as sintering aid for this material as it is the only variable among three powders.

3.2.4. Ionic conductivities

Fig. 12 provides a representative Nyquist plot of sintered LATSP pellets at 25°C . A depressed semicircle is observed at high frequencies followed by an inclined spike at lower frequencies. The semicircle is due to the sample's ionic conductivity, and the inclined spike to polarization of ion blocking electrodes [56]. While it is agreed that the semicircle corresponding to the grain resistance is not identifiable at room temperature for high conductivity materials as only one semicircle is present, some researchers argue that the left intercept of the semicircle with the real axis (Z') is grain resistance (R_g) and the diameter of the semicircle is the grain boundary resistance (R_{gb}) [26,31,32,35,57–59]. In contrast, others claim the left intercept is the circuit resistance external to the sample and the diameter of the semicircle is the total resistance ($R_t = R_g + R_{gb}$) [37,60–63]. Although the interpretations conflict, identical equivalent circuits are used for fitting, which was adopted here.

For the current study, since the left intercept was fairly small compared to the right intercept, the right intercept was taken as the total resistance as a conservative estimate. The equivalent circuit, presented in Fig. 12, was used to estimate total resistances. A single resistor (R_1) was used for the left intercept; a resistor (R_2) in parallel with a constant phase element (CPE_1) for the diameter of semicircle; and a constant phase element (CPE_2) for electrode polarization [41,56,57,60,64,65]. The total resistances were calculated as $R_1 + R_2$.

Fig. 13 depicts typical Nyquist plots of sintered LATSP pellets at 65° and 125°C . At 65°C , the semicircle is still identifiable although the diameter has greatly diminished compared to that at 25°C . Only a short arc is seen at 125°C .

Table 7 presents conductivities at 25°C and above. At 25°C , all samples show conductivities superior to $10^{-3} \text{ S cm}^{-1}$. The LATSP conductivity reported here, $2.4 \times 10^{-3} (\pm 7.6 \times 10^{-5}) \text{ S cm}^{-1}$, is about three times $7.7 \times 10^{-4} (\pm 1.5 \times 10^{-4}) \text{ S cm}^{-1}$, the highest value obtained in the preliminary studies. The major difference is the powder processing and cold isostatic pressing of the green pellets which eventually results in higher sintered densities. As a

Table 4
SSAs and APSs of LATSP and LATSP+10%.

	SSAs ($\text{m}^2 \text{ g}^{-1}$)	APSs (nm)
LATSP	40	56
LATSP+10%	35	64

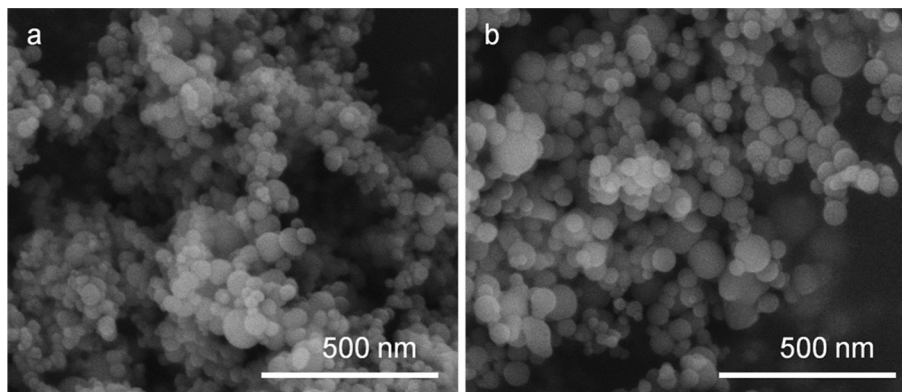


Fig. 8. SEM micrographs of as-produced a. LATSP and b. LATSP+10% nanopowders.

comparison, LATSP pellets sintered at 1100 °C for 1 h in the LATSP focused studies were 88 ± 1 %TD dense, whereas those sintered under identical heating conditions in the preliminary studies were 80 ± 1 %TD.

The total conductivities are on the order of 10^{-2} S cm $^{-1}$ at and above 65 °C, higher than the organic electrolyte conductivities at ambient. For example, LiClO $_4$ and LiPF $_6$ dissolved in organic solvents can have conductivities of 8.4×10^{-3} S cm $^{-1}$ and 1.1×10^{-2} S cm $^{-1}$ at 25 °C, respectively [21]. Temperatures near 65 °C are reached easily during battery operations as testified by the numerous built-in safety measures in organic electrolyte lithium batteries designed to limit temperature rises beyond 60 °C, which sometimes fail and result in permanent degradation or

thermal runaway caused by electrolyte decomposition and electrode/electrolyte reactions [12,21].

On another note, one can easily imagine batteries operating at 60–100 °C for HEV/EV/ESS applications due to the large battery volumes, hence, exhibiting lower thermal dissipation compared to small battery packs. Overall, LATSP seems to offer excellent potential for replacing organic electrolytes due to its high conductivities and much improved safety. Also, the low coefficients of thermal expansion (CTE) of LATP materials (7–11 ppm °C $^{-1}$) [35] suggests easier structural design of batteries compared to those using polyethylene oxide based polymer electrolytes (120 ppm °C $^{-1}$) [66] as the volume change during use at a range of temperature becomes less of a concern.

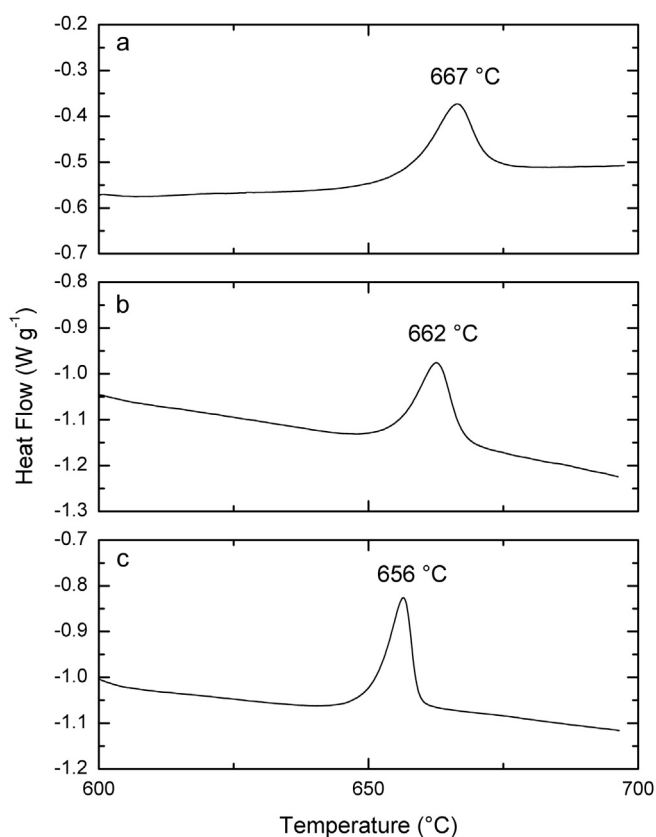


Fig. 9. DSC scans of a. LATSP, b. LATSP+5%, and c. LATSP+10% powder.

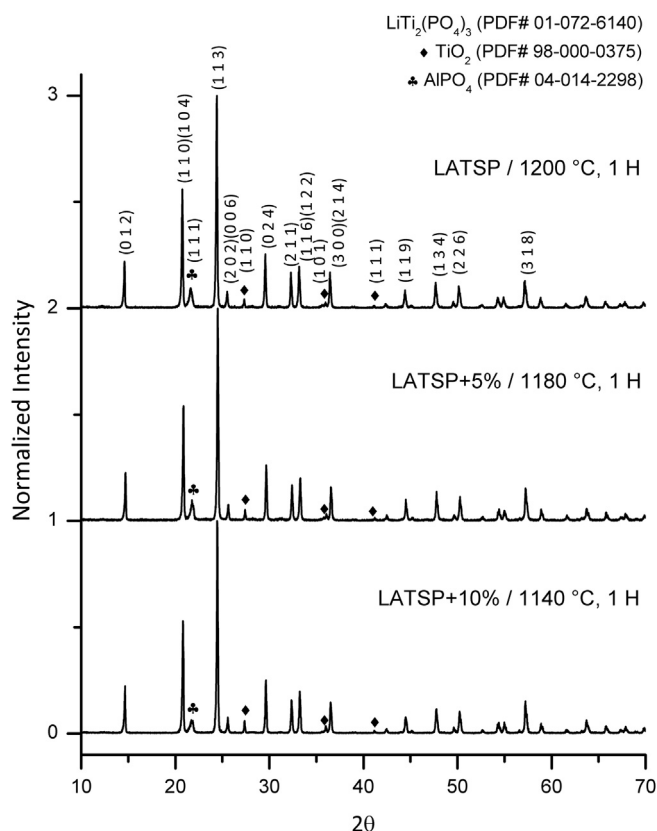


Fig. 10. XRD patterns of final, sintered pellets with the highest densities.

Table 5
Heating conditions, final densities, and phase compositions of sintered pellets.

	Heating conditions		Final density (% TD)	Phase compositions (wt%)		
	Crystallization	Sintering		LiTi ₂ (PO ₄) ₃	AlPO ₄	TiO ₂
LATSP	690 °C, 1 h	1200 °C, 1 h	93 ± 1	91 ± 0.5	7 ± 0.2	2 ± 0.5
LATSP+5%	680 °C, 1 h	1180 °C, 1 h	94 ± 1	91 ± 0.7	7 ± 0.5	2 ± 0.4
LATSP+10%	660 °C, 1 h	1140 °C, 1 h	94 ± 1	92 ± 0.4	5 ± 0.9	3 ± 0.6

Table 6
Lattice parameters of LATSP, LiTi₂(PO₄)₃, and Li_{1.3}Al_{0.3}Ti_{1.7}(PO₄)₃.

Sample	a (Å)	c (Å)
LATSP	8.5137(3)	20.8529(8)
LiTi ₂ (PO ₄) ₃ ^a	8.512	20.858
Li _{1.3} Al _{0.3} Ti _{1.7} (PO ₄) ₃ ^a	8.5	20.82

^a Ref. [25].

Fig. 14 shows selected temperature dependent measurements of Li⁺ ionic conductivities for all LATSP samples. Each plot exhibits an Arrhenius dependence. Conductivities at each temperature are within the error limits of each other such that no clear argument can be made on which exhibits higher conductivities. The activation energies derived from the slope of the Arrhenius plots are tabulated in Table 8. The Li⁺ diffusion mechanism is the same for all samples as there is no noticeable difference in activation energies. Conductivities and activation energies are comparable to those reported by Fu with similar compositions [40].

3.3. Thin film processing

Initial efforts were made to produce thin films that might offer similar properties in real devices given that commercially available solid membranes are 100–300 μm thick.

3.3.1. Green film analyses

In the Fig. 15 SEM fracture surface image of a green film, the LATSP+5% nanopowders seem to be well dispersed in the polymeric host. Obtaining crack free, green films using nanopowders is not an easy task. In general, high solids loadings of suspensions is preferential to minimize defect formation while drying the cast film. However, because nanopowder surfaces interact quite strongly with solvent, excess solvent is needed compared to micron sized particles.

One way of improving solids loadings is to start with low viscosity solvents [67,68]. For that matter, mixed solvent systems of ethanol/toluene, ethanol/xylene, and ethanol/methyl ethyl ketone are commonly used in tape casting. LATSP+5% does not disperse in toluene or xylene. Hence, an ethanol/methylethyl ketone system at

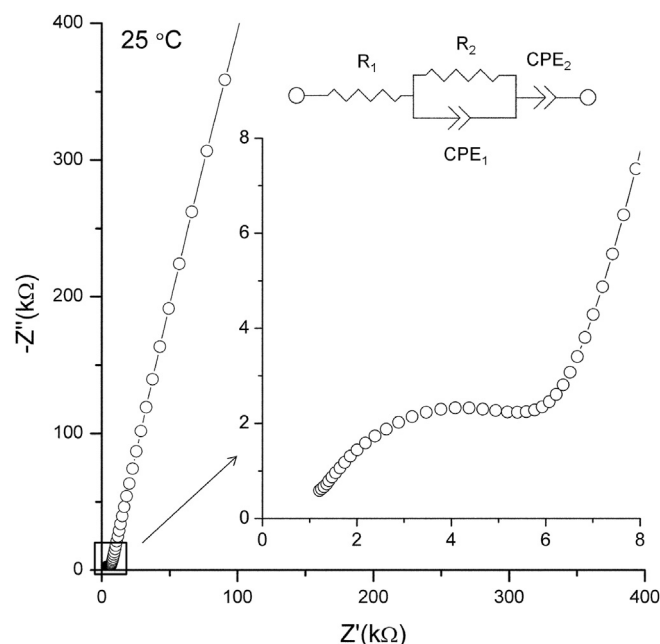


Fig. 12. Representative Nyquist plot for LATSP at 25 °C. Equivalent circuit used for fitting is presented. Inset shows high frequency region.

a volume ratio of 20/80 was used to obtain crack free, green films on drying.

Another method of reducing viscosity, thereby increasing solids loading for a given suspension, is to add dispersants [62,63,69,70]. Polyacrylic acid at 3 wt % with respect to powder mass, was used in the current studies. Optimal dispersant and solvent volume ratios were determined empirically.

From Table 2, the expected ceramic yields of processed green films can be calculated as 77 wt% (57 vol%), excluding solvent as it evaporates on drying. The Fig. 16 TGA/DSC shows the green film to have a ceramic yield identical to theory. Two exotherms are seen accompanied by mass losses at intermediate temperatures from decomposition of polymeric additives: polyacrylic acid, benzylbutyl phthalate, and polyvinyl butyral. The mass loss ceases at ~500 °C and a LiTi₂(PO₄)₃ crystallization exotherm is observed at 662 °C, consistent with as-produced powder analyses in Fig. 9. The endotherm spike at 600 °C is due to a change in ramp rate.

3.3.2. Sintered film analyses

Sintering temperatures were limited to 1000 °C as higher temperatures caused films to sinter onto the alumina plates used as substrates. Fig. 17 shows optical and SEM fracture surface images of a film sintered to 1000 °C/1 h. The film thickness is 52 ± 1 μm. Pores

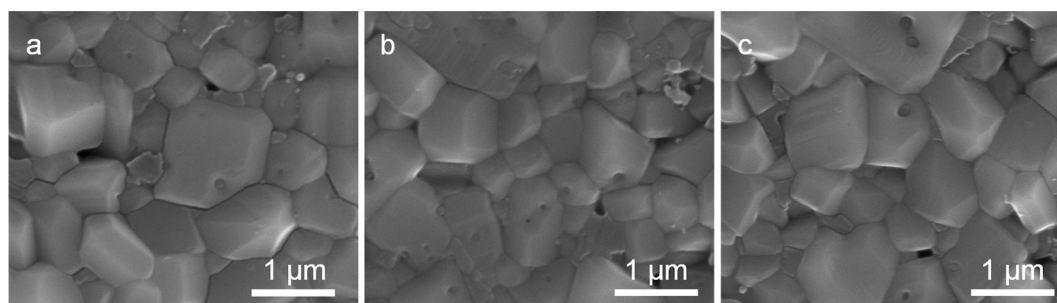


Fig. 11. Polished and thermally etched pellet surfaces of a. LATSP, b. LATSP+5%, and c. LATSP+10%.

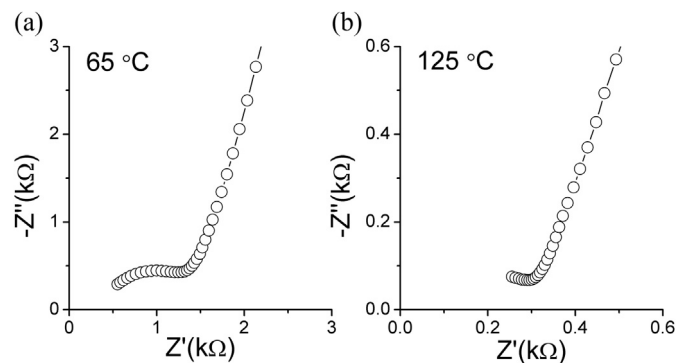


Fig. 13. Representative Nyquist plots for LATSP at a. 65°, and b. 125 °C. The high frequency regions are shown.

are observed in the microstructure indicating % TD is lower compared to the above described pellet samples. Sintered films offer densities of $88 \pm 1\%$ of theory, roughly 6% lower than pellets sintered at optimal sintering schedules per above. This is expected as optimal sintering conditions as specified in Table 5 could not be adopted for thin film sintering as a consequence of adhesion to substrates.

Fig. 18 provides an XRD of a sintered film. All major peaks correspond to $\text{LiTi}_2(\text{PO}_4)_3$. Small amounts of AlPO_4 and TiO_2 secondary phases are present.

Fig. 19 presents a typical Nyquist plot for sintered films at 25 °C. The Nyquist plot of the as-sintered films shows what seems to be a portion of a semicircle. We suspect this is due to mild deposition of alumina onto the film, thereby reducing the effective electrode area when sputter coated. Note that the total resistance is inversely proportional to the electrode area if the total conductivity is fixed. Furthermore, with the film sintering onto the alumina substrate at higher temperatures, it is reasonable to assume mild deposition at 1000 °C. After gently grinding the surface of the sintered films with 1200 grit SiC paper, the impedance behavior becomes very different per Fig. 19b, thereby proving there are unwanted impurities on the as-sintered film surfaces.

The obtained total conductivities of surface ground films are $4.3 \times 10^{-4} (\pm 1.4 \times 10^{-4}) \text{ S cm}^{-1}$ at ambient, fairly low compared to pellet conductivities ($>10^{-3} \text{ S cm}^{-1}$). This can mainly be attributed to lower final densities of 88 % TD. Table 9 compares thicknesses and room temperature conductivities of the LATSP films to commercially available products and to what other groups have reported. The total conductivity of LATSP+5% film is comparable to other values listed in Table 9. Note all films below 100 μm were tape cast. Glass-ceramic sheets were ball-milled to obtain feedstock for tape casting [36,38]. A sol–gel processing study required calcination for complete reaction resulting in aggregates that necessitated high energy mechanical milling before or during suspension formulation to break them down [59,71]. Only LF–FSP alone provides nanopowders that can be directly used for tape casting when

Table 7

Total conductivities (σ_t) of LATSP samples at selected temperatures.

T (°C)	σ_t (S cm^{-1})		
	LATSP	LATSP+5%	LATSP+10%
25	2.4×10^{-3}	2.9×10^{-3}	2.1×10^{-3}
45	5.5×10^{-3}	6.6×10^{-3}	4.9×10^{-3}
65	1.1×10^{-2}	1.3×10^{-2}	1.0×10^{-2}
85	2.0×10^{-2}	2.2×10^{-2}	1.9×10^{-2}
105	3.3×10^{-2}	3.4×10^{-2}	3.1×10^{-2}
125	5.1×10^{-2}	5.4×10^{-2}	4.9×10^{-2}

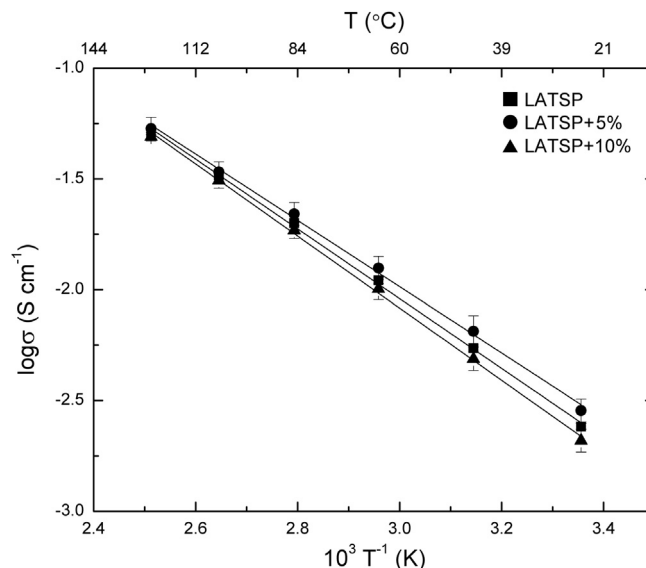


Fig. 14. Arrhenius plots of LATSP, LATSP+5%, and LATSP+10%.

Table 8

Activation energies of LATSP, LATSP+5%, and LATSP+10%.

Sample	E_a (σ_t) (kJ mol^{-1})
LATSP	30.1 ± 0.3
LATSP+5%	28.6 ± 0.3
LATSP+10%	31.1 ± 0.8

producing thin films ($<100 \mu\text{m}$). LAGP materials which Ge is substituting Ti of LATP show high conductivities but may not be suitable for commercialization due to the higher cost of Ge.

The optimization of film processing and sintering conditions to reach conductivities similar to those observed in pellet samples at $10^{-3} \text{ S cm}^{-1}$ remains as future work. Increasing the solids loading of green films hence starting with a higher % TD, extended sintering times, sintering in a Li_2O vapor environment or using different substrates during sintering are under exploration. The mechanical

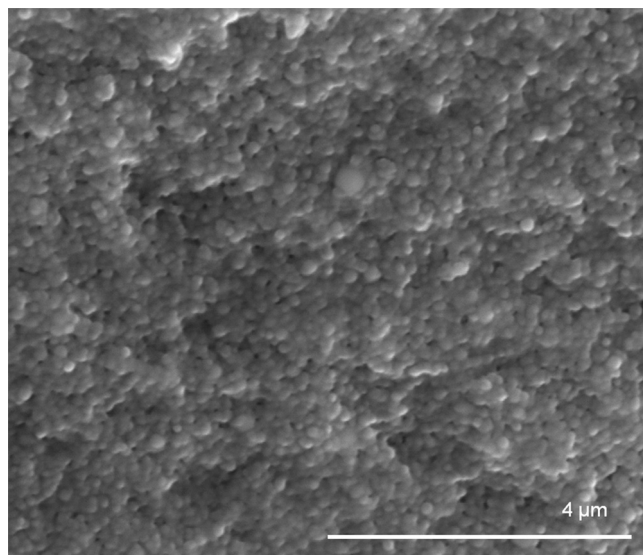


Fig. 15. SEM fracture surface image of green film.

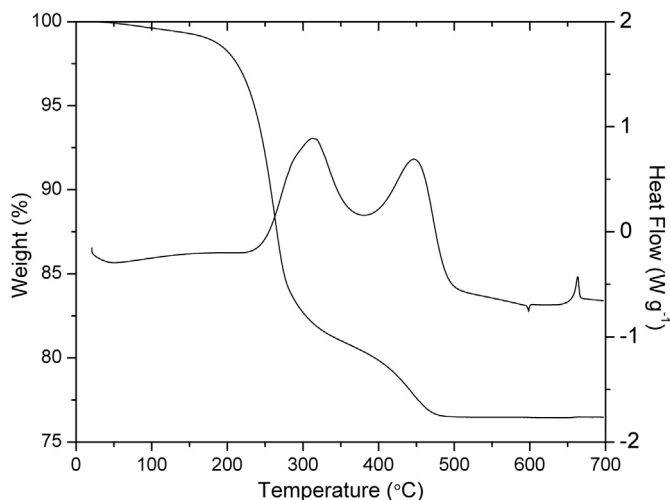


Fig. 16. TGA/DSC of green film.

strength and cyclic voltammetry of such films will be measured as well.

4. Conclusions

$\text{Li}_{1.7}\text{Al}_{0.3}\text{Ti}_{1.7}\text{Si}_{0.4}\text{P}_{2.6}\text{O}_{12}$ pellets showed the highest ionic conductivities of 7.7×10^{-4} ($\pm 1.5 \times 10^{-4}$) S cm^{-1} among the $\text{Li}_{1+x+y}\text{Al}_x\text{Ti}_{2-x}\text{Si}_y\text{P}_{3-y}\text{O}_{12}$ ($x = 0.1, 0.3/y = 0.2, 0.4$) compositions in preliminary studies. Improving the green densities resulted in $\text{Li}_{1.7}\text{Al}_{0.3}\text{Ti}_{1.7}\text{Si}_{0.4}\text{P}_{2.6}\text{O}_{12}$ pellets with superionic conductivities of 2.4×10^{-3} ($\pm 7.6 \times 10^{-5}$) S cm^{-1} at room temperature when sintered. Adding 5 and 10 wt% of excess lithium lowered both crystallization points and sintering temperatures by 5 ± 1 °C and 20 ± 5 °C respectively for 5 wt%, and 11 ± 1 °C and 60 ± 5 °C respectively for 10 wt% of excess lithium. However, no noticeable effects on the conductivities were observed.

Low activation energies (30 ± 1 kJ mol $^{-1}$), small grain sizes (600 ± 200 nm), high Li concentrations of 1.7, and high final densities ($94 \pm 1\%$ TD) combine to offer superionic conductivities in LATSP/LATSP+5%/LATSP+10% pellets. The obtained room temperature conductivities are comparable to the superionic conductivities reported by glass-ceramic processing method. High room temperature conductivities coupled with conductivities of 10^{-2} S cm^{-1} only at 60 °C suggests LATSP to be an excellent candidate material for replacing organic liquid electrolytes, thereby improving safety as well.

Initial thin film processing studies using LF-FSP nanopowders were successful, proving their direct utility for tape casting, unlike

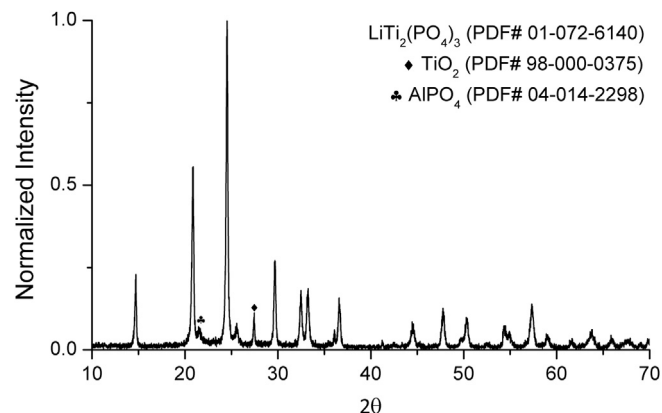
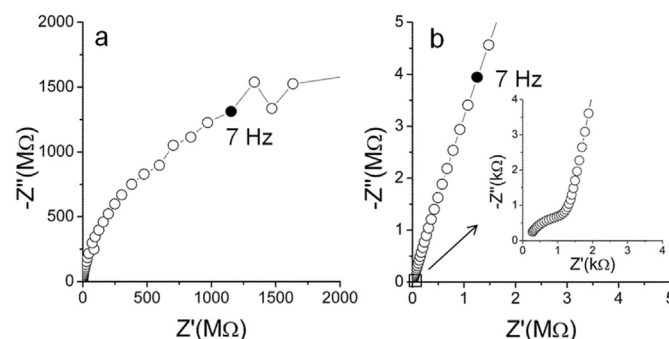
Fig. 18. XRD pattern of films sintered at 1000 °C/1 h. Peaks with no label correspond to $\text{LiTi}_2(\text{PO}_4)_3$.

Fig. 19. Nyquist plots of a. as-sintered, and b. surface ground films.

Table 9

Reported room temperature conductivities for NASICON structured membranes.

	Processing step	σ_t (S cm^{-1})	Thickness (μm)	Reference
LATSP+5%	LF-FSP/TC	4.3×10^{-4}	52	—
OHARA Inc. LATP	GC/P	1×10^{-4}	150	[57,72]
$\text{Li}_{1.3}\text{Al}_{0.3}\text{Ti}_{1.7}(\text{PO}_4)_3$	GC/BM/TC	1.8×10^{-4}	40	[38]
$\text{Li}_{1.4}\text{Al}_{0.4}\text{Ge}_{1.6}(\text{PO}_4)_3$	SG/C/TC	3.4×10^{-4}	75	[59]
$\text{Li}_{1.4}\text{Al}_{0.4}\text{Ge}_{1.6}(\text{PO}_4)_3$	SG/C/TC	8.4×10^{-4}	200	[71]
$\text{Li}_{1.5}\text{Al}_{0.5}\text{Ge}_{1.5}(\text{PO}_4)_3$	GC/BM/TC	6.4×10^{-4}	200	[36]

GC = glass-ceramic, SG = sol-gel, C = calcination, BM = ball-milling, TC = tape casting, P = polishing.

glass-ceramic or sol-gel processing methods. Obtained thin film conductivities of 4.3×10^{-4} ($\pm 1.4 \times 10^{-4}$) S cm^{-1} are comparable to what other groups have reported with similar materials per Table 9. The conductivity disparities between the films and the pellets are

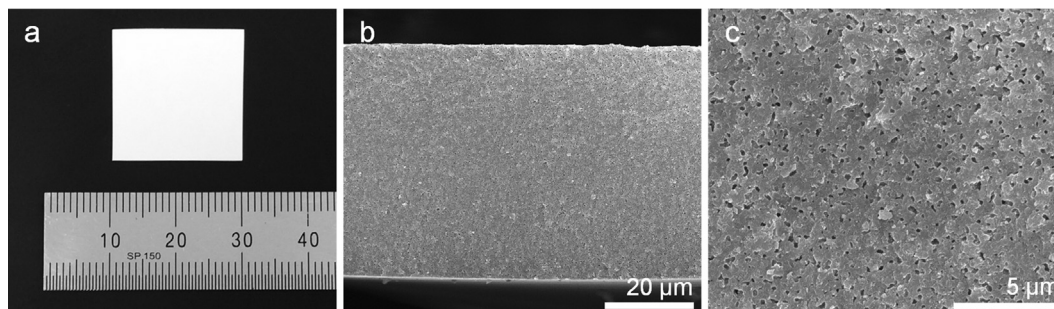


Fig. 17. a. optical and b/c. SEM fracture surface images of sintered film.

ascribed to films' lower final densities (88 ± 1 %TD) vs 94 ± 1 % in the pellets. Future work remains to match the film conductivities seen for pellets.

The work presented here strongly suggests that the materials and thin films made from them offer excellent potential to supplant liquid electrolytes in a wide variety of Li based batteries. Furthermore, ceramics have very high tolerance to heat suggesting safety at higher operating temperatures offering superior charge/discharge rates, as failure mechanisms common to liquid electrolytes are not present.

Acknowledgment

The work discussed above was partially supported by Quallion LLC. We also would like to thank NSF for partial support of the work through DMR grant 1105361. The research reported here was conceived and implemented by R. Tamaki, E. Yi and R. M. Laine. Selected impedance measurements were conducted in part by S. Mohanty. Detailed impedance measurements at UM were conducted by W. Wang and J. Kieffer with support from NSF grant DMR-1106058. RML would like to thank the Technion, Haifa, Israel for a Lady Davis Fellowship where portions of this manuscript were written.

References

- [1] P.G. Bruce, B. Scrosati, J.-M. Tarascon, *Angew. Chem. Int. Ed.* 47 (2008) 2930–2946.
- [2] J.-M. Tarascon, M. Armand, *Nature* 414 (2001) 359–367.
- [3] M. Armand, J.-M. Tarascon, *Nature* 451 (2008) 652–657.
- [4] K.M. Abraham, *Electrochim. Acta* 38 (1993) 1233–1248.
- [5] B. Scrosati, J. Garche, *J. Power Sources* 195 (2010) 2419–2430.
- [6] M.-K. Song, S. Park, F.M. Alamgir, J. Cho, M. Liu, *Mater. Sci. Eng. R* 72 (2011) 203–252.
- [7] T.-H. Kim, J.-S. Park, S.-K. Chang, S. Choi, J.H. Ryu, H.-K. Song, *Adv. Energy Mater.* 2 (2012) 860–872.
- [8] B. Scrosati, J. Hassoun, Y.-K. Sun, *Energy Environ. Sci.* 4 (2011) 3287–3295.
- [9] J.W. Fergus, *J. Power Sources* 195 (2010) 4554–4569.
- [10] U.V. Sacken, E. Nodwell, A. Sundher, J.R. Dahn, *Solid State Ionics* 69 (1994) 284–290.
- [11] S.-I. Tobishima, J.-I. Yamaki, *J. Power Sources* 81–82 (1999) 882–886.
- [12] P.G. Balakrishnan, R. Ramesh, T.P. Kumar, *J. Power Sources* 155 (2006) 401–414.
- [13] S.S. Zhang, *J. Power Sources* 164 (2007) 351–364.
- [14] T.D. Hatchard, D.D. MacNeil, D.A. Stevens, L. Christensen, J.R. Dahn, *Electrochem. Solid-State Lett.* 3 (2000) 305–308.
- [15] M.A. Gee, F.C. Laman, *J. Electrochem. Soc.* 140 (1993) L53–L55.
- [16] W.H. Meyer, *Adv. Mater.* 10 (1998) 439–448.
- [17] F. Groce, G.B. Appetecchi, L. Persi, B. Scrosati, *Nature* 394 (1998) 456–458.
- [18] Y. Sun, *Nano Energy* 2 (2013) 801–816.
- [19] N. Anantharamulu, K.K. Rao, G. Rambabu, B.V. Kumar, V. Radha, M. Vithal, *J. Mater. Sci.* 46 (2011) 2821–2837.
- [20] J.T. Dudley, D.P. Wilkinson, G. Thomas, R. LeVae, S. Woo, H. Blom, C. Horvath, M.W. Juskow, B. Denis, P. Juric, P. Aghakian, J.R. Dahn, *J. Power Sources* 35 (1991) 59–82.
- [21] K. Xu, *Chem. Rev.* 104 (2004) 4304–4417.
- [22] G. Nuppl, T. Takeuchi, A. Weiß, H. Kageyama, K. Yoshizawa, T. Yamabe, *J. Appl. Phys.* 86 (1999) 5484–5491.
- [23] L.-O. Hagman, P. Kierkegaard, *Acta Chem. Scand.* 22 (1968) 1822–1832.
- [24] A. Aatiq, M. Ménétrier, L. Croguennec, E. Suard, C. Delmas, *J. Mater. Chem.* 12 (2002) 2971–2978.
- [25] H. Aono, E. Sugimoto, Y. Sadaoka, N. Imanaka, G.-Y. Adachi, *J. Electrochem. Soc.* 137 (1990) 1023–1027.
- [26] D. Popovici, H. Nagai, S. Fujishima, J. Akedo, *J. Am. Ceram. Soc.* 94 (2011) 3847–3850.
- [27] K. Arbi, S. Mandal, J.M. Rojo, J. Sanz, *Chem. Mater.* 14 (2002) 1091–1097.
- [28] J. Fu, *Solid State Ionics* 96 (1997) 195–200.
- [29] C.-M. Chang, Y.I. Lee, S.-H. Hong, *J. Am. Ceram. Soc.* 88 (2005) 1803–1807.
- [30] M. Forsyth, S. Wong, K.M. Nairn, A.S. Best, P.J. Newman, D.R. MacFarlane, *Solid State Ionics* 124 (1999) 213–219.
- [31] Z. Wen, X. Xu, J. Li, *J. Electroceram.* 22 (2009) 342–345.
- [32] X. Xu, Z. Wen, X. Yang, J. Zhang, Z. Gu, *Solid State Ionics* 177 (2006) 2611–2615.
- [33] S. Wong, P.J. Newman, A.S. Best, K.M. Nairn, D.R. MacFarlane, M. Forsyth, *J. Mater. Chem.* 8 (1998) 2199–2203.
- [34] P. Maldonado-Manso, E.R. Losilla, M. Martínez-Lara, M.A.G. Aranda, S. Bruque, F.E. Mouahid, M. Zahir, *Chem. Mater.* 15 (2003) 1879–1885.
- [35] S.D. Jackman, R.A. Cutler, *J. Power Sources* 218 (2012) 65–72.
- [36] J.S. Thokchom, N. Gupta, B. Kumar, *J. Electrochem. Soc.* 155 (2008) A915–A920.
- [37] B. Kumar, D. Thomas, J. Kumar, *J. Electrochem. Soc.* 156 (2009) A506–A513.
- [38] L. Puech, C. Cantau, P. Vinatier, G. Toussaint, P. Stevens, *J. Power Sources* 214 (2012) 330–336.
- [39] J.S. Thokchom, B. Kumar, *J. Electrochem. Soc.* 154 (2007) A331–A336.
- [40] J. Fu, *J. Am. Ceram. Soc.* 80 (1997) 1901–1903.
- [41] P. Johnson, N. Sammes, N. Imanishi, Y. Takeda, O. Yamamoto, *Solid State Ionics* 192 (2011) 326–329.
- [42] S. Li, C. Xian, K. Yang, C. Sun, Z. Wang, L. Chen, *J. Power Sources* 205 (2012) 57–62.
- [43] J.D. Nicholas, L.C. De Jonghe, *Solid State Ionics* 178 (2007) 1187–1194.
- [44] S. Le, S. Zhu, X. Zhu, K. Sun, *J. Power Sources* 222 (2013) 367–372.
- [45] A.C. Sutorik, S.S. Neo, D.R. Treadwell, R.M. Laine, *J. Am. Ceram. Soc.* 81 (1998) 1477–1486.
- [46] R. Baranwal, M.P. Villar, R. Garcia, R.M. Laine, *J. Am. Ceram. Soc.* 84 (2001) 951–961.
- [47] C. R. Bickmore, K.F. Waldner, R. Baranwal, T. Hinklin, D.R. Treadwell, R.M. Laine, *J. Eur. Ceram. Soc.* 18 (1998) 287–297.
- [48] J. Marchal, T. John, R. Baranwal, T. Hinklin, R.M. Laine, *Chem. Mater.* 16 (2004) 822–831.
- [49] T. Hinklin, B. Tourny, C. Gervais, F. Babonneau, J.J. Gislason, R.W. Morton, R.M. Laine, *Chem. Mater.* 16 (2004) 21–30.
- [50] A.S. Bondarenko, G.A. Ragoisha, in: A.L. Pomerantsev (Ed.), *Progress in Chemometrics Research*, Nova Science Publishers, New York, 2005, pp. 89–102 the program is available online at: <http://www.abc.chemistry.bsu.by/vi/analyser/>.
- [51] J.S. Thokchom, B. Kumar, *Solid State Ionics* 177 (2006) 727–732.
- [52] K. Nagata, T. Nanno, *J. Power Sources* 174 (2007) 832–837.
- [53] B. Key, D.J. Schroeder, B.J. Ingram, J.T. Vaughey, *Chem. Mater.* 24 (2012) 287–293.
- [54] C.R. Mariappan, C. Yada, F. Rosciano, B. Roling, *J. Power Sources* 196 (2011) 6456–6464.
- [55] R.D. Shannon, *Acta Crystallogr.* A32 (1976) 751–767.
- [56] P.G. Bruce, A.R. West, *J. Electrochem. Soc.* 130 (1983) 662–669.
- [57] N. Imanishi, S. Hasegawa, T. Zhang, A. Hirano, Y. Takeda, O. Yamamoto, *J. Power Sources* 185 (2008) 1392–1397.
- [58] K. Kim, J. Kim, Y. Yoon, D. Shin, *Met. Mater. Int.* 20 (2014) 189–194.
- [59] M. Zhang, Z. Huang, J. Cheng, O. Yamamoto, N. Imanishi, B. Chi, J. Pu, J. Li, *J. Alloys Compd.* 590 (2014) 147–152.
- [60] H.S. Jadhav, M.-S. Cho, R.S. Kalubarme, J.-S. Lee, K.-N. Jung, K.-H. Shin, C.-J. Park, *J. Power Sources* 241 (2013) 502–508.
- [61] C.R. Mariappan, M. Gellert, C. Yada, F. Rosciano, B. Roling, *Electrochem. Commun.* 14 (2012) 25–28.
- [62] J.S. Thokchom, B. Kumar, *J. Power Sources* 185 (2008) 480–485.
- [63] J.S. Thokchom, B. Kumar, *J. Power Sources* 195 (2010) 2870–2876.
- [64] Y. Deng, S.-J. Shang, A. Mei, Y.-H. Lin, L.-Y. Liu, C.-W. Nan, *J. Alloys Compd.* 472 (2009) 456–460.
- [65] A. Mei, X.-L. Wang, Y.-C. Feng, S.-J. Zhao, G.-J. Li, H.-X. Geng, Y.-H. Lin, C.-W. Nan, *Solid State Ionics* 179 (2008) 2255–2259.
- [66] Y. Rao, T.N. Blanton, *Macromolecules* 41 (2008) 935–941.
- [67] V. Vinodhini, P. Singh, M. Balasubramanian, *J. Mater. Sci.* 41 (2006) 7082–7087.
- [68] S. Bhaskar Reddy, P. Paramanano Singh, N. Raghu, V. Kumar, *J. Mater. Sci.* 37 (2002) 929–934.
- [69] A.K. Maiti, B. Rajender, *Mater. Sci. Eng. A* 333 (2002) 35–40.
- [70] E. Yi, J.C. Furgal, J. Azurdia, R.M. Laine, *J. Mater. Chem. A* 2 (2014) 3766–3775.
- [71] M. Zhang, K. Takahashi, I. Uechi, Y. Takeda, O. Yamamoto, D. Im, D.-J. Lee, B. Chi, J. Pu, J. Li, N. Imanishi, *J. Power Sources* 235 (2013) 117–221.
- [72] T. Zhang, N. Imanishi, S. Hasegawa, A. Hirano, J. Xie, Y. Takeda, O. Yamamoto, N. Sammes, *Electrochem. Solid-State Lett.* 12 (2009) A132–A135.